frontiers | Frontiers in Materials

TYPE Review
PUBLISHED 16 April 2024
DOI 10.3389/fmats.2024.1381818

OPEN ACCESS

EDITED BY
Hongliang Zhang,
Fudan University, China

REVIEWED BY
Corey Efaw,
Boise State University, United States
Guanze He,
Shanghai Nuclear Engineering Research and Design Institute, China

*CORRESPONDENCE
Di Yun,
diyun1979@xjtu.edu.cn

RECEIVED 04 February 2024
ACCEPTED 29 March 2024
PUBLISHED 16 April 2024

CITATION
Tang Y, Liao J and Yun D (2024), Understanding the high-temperature corrosion behavior of zirconium alloy as cladding tubes: a review.
Front. Mater. 11:1381818.
doi: 10.3389/fmats.2024.1381818

Understanding the high-temperature corrosion behavior of zirconium alloy as cladding tubes: a review

Yan Tang[1], Jingjing Liao[1] and Di Yun[2]*

[1]Science and Technology on Reactor Fuel and Materials Laboratory, Nuclear Power Institute of China, Chengdu, China, [2]School of Nuclear Science and Technology, Xi'an Jiaotong University, Xi'an, China

Operated under extreme conditions, corrosion occurs between zirconium alloy cladding tubes and the coolant in the primary loop of pressurized water reactors (PWRs), contributing to a reduction in the effective metallic material thickness. Therefore, understanding the corrosion behavior of zirconium alloy is vital to both raising the burnup of PWR and the improvement of safety properties of these reactors. During the past decades, extensive investigation was conducted with various conditions, such as changing corrosion temperatures and alloying elements, but contradiction persists and universal conclusion remain elusive. In the present work, a variety of research results that focused on corrosion kinetics, microstructural evolution, and the influence of alloying elements were integrated and summarized, so that a valuable reference can be provided to further research.

KEYWORDS

zirconium alloy, high temperaature oxidation, corrosion, kinetic transition, alloying element

1 Introduction

The aggravation of global climate issues increases the public attention on clean energy, especially for the nuclear energy, known for its controllability and sustainability. Safety consideration, particularly in the aftermath of events like the Fukushima nuclear disaster, is given the priority, even over the financial efficiency. As the first safety barrier of nuclear reactor, the integrity of cladding tubes is essential to prevent the leakage of radioactive products under both normal operating or accident conditions. Correspondingly, zirconium alloy, due to its low neutron absorption cross section (0.18×10^{-28} m^2), is the only commercial materials for cladding tubes. In reactors, zirconium alloys are exposed to extreme conditions, typically 360°C and 15.5 MPa at coolant-side, and the aggressive chemistry, usually containing boron and lithium. This exposure leads to electrochemical interactions between zirconium alloy and coolant in the main loop. Associated studies indicate that these interactions accelerate under higher burnup conditions or during accidents (Park et al., 2010; Allen et al., 2012a; Lee et al., 2017).

There are two main degradation processes: corrosion transition and hydrogen pickup. The corrosion transition (i.e., breakaway phenomenon) refers to an acceleration in corrosion rate (Cox, 2005; Park et al., 2007; Ni et al., 2012; Baek and Jeong, 2008; Leistikow and Schanz, 2022), resulting in a reduction of the effective oxide thickness and the failure of the protective oxide film. In parallel with corrosion, hydrogen, produced during corrosion, ingresses into the zirconia matrix. The low solubility for hydrogen [about 80 ppm by wt

at 300°C and 200 ppm by wt at 400°C (Allen et al., 2012a)], can lead to its precipitation as hydrides, negatively affecting mechanical properties, such as embrittlement, delayed hydride cracking, and loss of fracture strength (Allen et al., 2012b). Therefore, no matter aiming to enhance burnup or safety properties, it is salient to understand the corrosion mechanism and improve the corrosion resistance.

The investigation of zirconium alloy corrosion in nuclear energy application can be traced back to the 1960s. The diverse range of exposed temperatures [300°C–1,600°C (Garzarolli et al., 1996; Arima et al., 2004; Park et al., 2007; Leistikow and Schanz, 2022; Sun et al., 2020; Liu et al., 2021)], and alloy elements, including Cr, Fe, Ni, Nb, Sn, and Cu, complicates predictions and explanations of corrosion behavior. While a variety of mechanisms on corrosion transition, such as zirconia (ZrO_2) transformation from tetragonal phase to monoclinic phase (t-m transformation) (Qin et al., 2006; Wei et al., 2013) or the porosity of oxide (Ni et al., 2010; Hu et al., 2019; Cui et al., 2022; Cui et al., 2024), have been proposed, contradictions persist and a universal conclusion remains elusive. Given the complexity of zirconium alloy corrosion behavior, integration and summary of previous research results are imperative. This review provides a comprehensive understanding of corrosion mechanisms, pave the way for further research, and offer guidance for the design of new zirconium alloy compositions with improved corrosion resistance.

2 Corrosion mechanisms and kinetics

2.1 Corrosion mechanism

At high temperature, zirconium interacts with water as follow:

$$Zr + 2H_2O \rightarrow ZrO_2 + H_2$$

The mobility of zirconium ion, Zr^{4+}, is expected to be extremely low, as evidenced by its immobility during the growth of anodic oxide film (Cox and Pemsler, 1968). This characteristic makes oxygen ions, O^{2-}, the only mobile species in the corrosion system. However, Whitton, (1968) also proposed that, at a relatively high temperature, such as a loss-of-coolant accident (LOCA) condition, there might be some migration of small zirconium ions. To maintain the charge neutrality of the system, an electron flux moving in the opposite direction is required. As an ionic oxide without available free electrons, it is believed that the transformation of oxygen ions is achieved through vacancies (V_O'') (Cox and Pemsler, 1968; Allen et al., 2012a) in the system, through either bulk diffusion or grain boundary diffusion (Cox and Pemsler, 1968). Cox and Pemsler, (1968) used radioactive oxygen measurements and found that bulk diffusion is over five orders of magnitude slower than grain boundary diffusion, which means that grain boundary is the dominant diffusion path. It should be noted that, as an element belonging to Group IV, zirconium accommodates a large amount of oxygen (Pieraggi et al., 1995). Therefore, the weight gain of zirconium corrosion comprises two parallel processes (Zino et al., 2021), the formation of oxide and the solid solution of oxygen (Pieraggi et al., 1995; Zino et al., 2021), as illustrated in Figure 1.

2.2 Corrosion kinetics

The Research on corrosion behavior of zirconium alloys has predominantly focused on temperatures ranging from 300°C to 1,400°C. Due to the dominant application of pressurized water reactors (PWRs), extensive investigation aims to the corrosion mechanism at the operating condition of PWRs, where the coolant-side temperature is 360°C. The occurrence of Fukushima Nuclear Disaster also attracts public attention to the corrosion behavior at higher temperature. When loss-of-coolant accident (LOCA) happens, the rapid depressurization in main loop caused by facture of pipes leads to evaporation of coolant, which generates steam as corrosion medium. At the same time, cladding tubes experience a dramatic temperature increase to over 1,000°C due to the loss of coolant. Therefore, the corrosion experiments exceeding 1,000°C is designed to simulate LOCA in PWRs. Moreover, research around 500°C, aimed for the nodular corrosion observed in the boiling water reactors (BWRs) (Charquet, 2001; Xie et al., 2017; Samanta et al., 2023).

Under operating condition, it is commonly observed that there are three stages of corrosion (Wei et al., 2013; Cui et al., 2022), as shown in Figure 2A. The pre-transition stage demonstrates cubic law kinetics governed by the Wagner rule (Wagner, 1933), followed by the transitory stage composed by a set of successive cubic curves. Finally, corrosion enters the post-transition stage where the weight gain curve increases linearly with time. As temperature increases, the occurrence of transition is much earlier, and the corrosion only contains two stages, as shown in Figure 2B. The initial stage obeying a cubic or parabolic law would transform to a quasi-linear subsequent stage.

Nagase et al. (2003) performed experiments in the temperature range of 500–1,300°C, and found a quasi-cubic law with an exponent n around 2.5–3 when temperature is lower than 900°C, as shown in Figure 2C. When temperature exceeds 1,000°C (1273K), the cubic law completely transforms into a parabolic law. The authors suggested that this transformation results from the stabilization of tetragonal phase of ZrO_2 (t-ZrO_2) at higher temperature. Apart from the oxidation exponent, the increased temperature can also significantly shorten the time required by breakaway phenomenon. For example, 180 days is needed at 360°C (Wei et al., 2013), while only 20 min is needed at 1,000°C (Cui et al., 2022). Meanwhile, as temperature increases, α-Zr with a close-packed hexagonal structure transform to β-Zr (cubic structure) (Wilhelm and Garcia, 1987; Lee et al., 2017). The oxygen, as a stabilizing α phase element, forces β-Zr near the oxide-metal interface to be converted to α-Zr and, thus, leads to a layer of α-Zr(O) phase underneath the oxide-metal interface (Kim et al., 2011).

3 The microstructure of oxide film

As corrosion proceeds, there are significant changes in grain morphology and lattice structure. Meanwhile, the appearance of porosity and cracks in the oxide film was also reported as the oxide grains moves far away from the oxide-metal (O-M) interface.

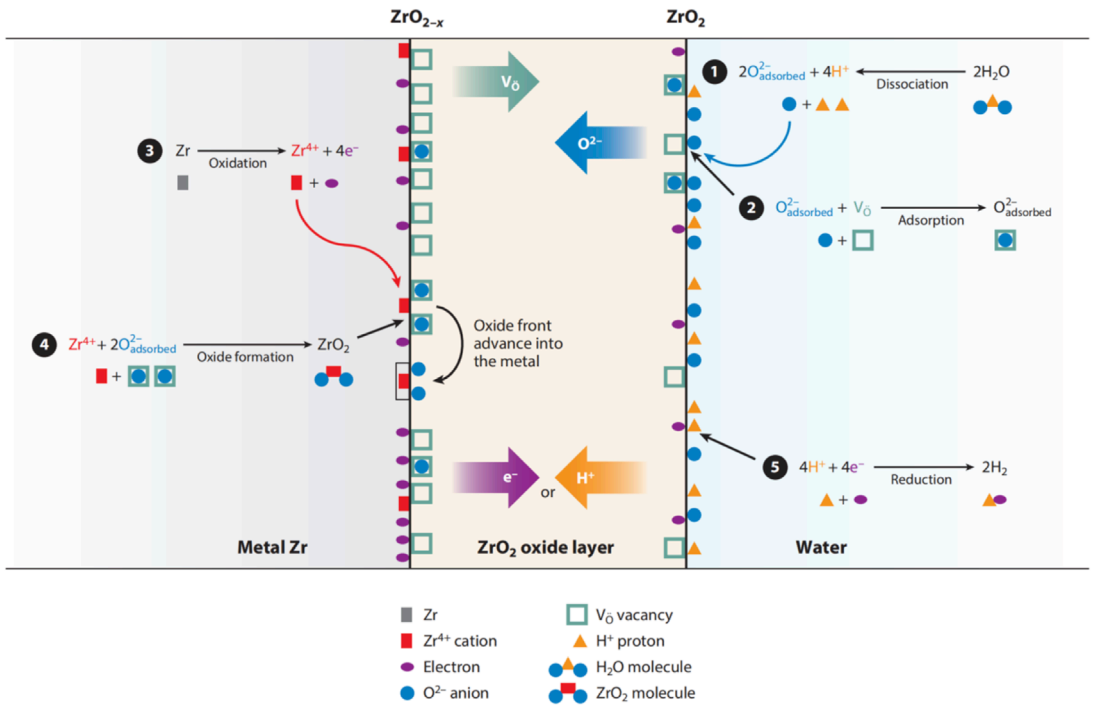

FIGURE 1
Schematic of corrosion process in zirconium alloys (Motta et al., 2015).

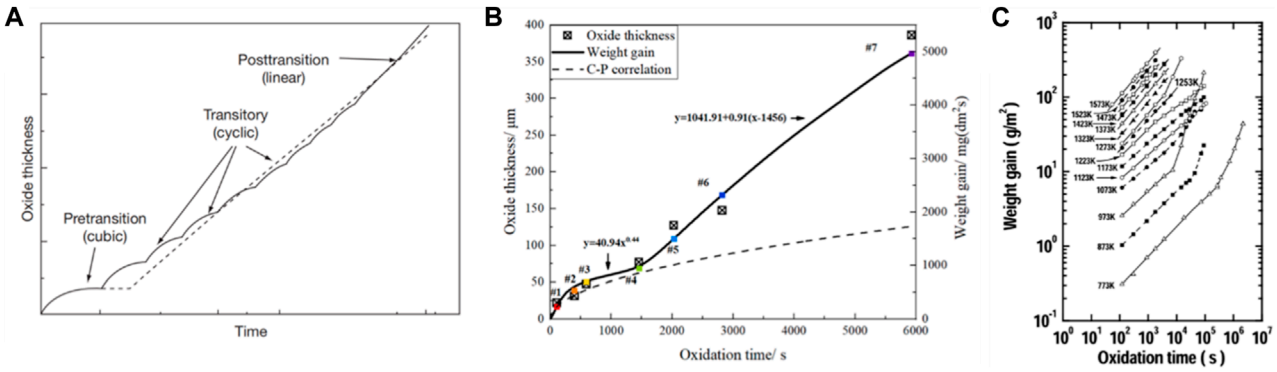

FIGURE 2
(A) Schematic representation of zirconium alloy corrosion (Allen et al., 2012a), **(B)** Weight gain curve obtained at 1,000°C using synchrotron thermogravimetric analyzer (STA) (Cui et al., 2022), **(C)** Weight gain obtained by NAGASE et al. (2003) at temperatures of 773K through 1,573K.

3.1 Morphology and structure of oxide

The morphology of oxide grains has been comprehensively investigated using various electron microscopy techniques. In the early stage of corrosion, small equiaxed oxide grain form and grow anisotropically into columnar grains (Jeong et al., 1999; Yilmazbayhan et al., 2006), as depicted in Figure 3. The strong texture and compact arrangement of these columnar grains contribute to the protective nature of oxide film. However, at the coolant-side of oxide film, the dense columnar grains transform into the loose and porous equiaxed grains, as shown inFigure 3. This transformation leads to the degradation of the film's protective function.

Apart from morphology changes, the structure of oxide also undergoes transformation over time. At the service temperature, the monoclinic phase of ZrO_2 is the only thermodynamically stable phase (Setiadinata, 2016), exhibiting over six different structures dependent on temperature and pressure (Whitney, 1965; BLOCK et al., 1985; Ohtaka et al., 1988; Ohtaka et al., 1990; Ohtaka et al., 1991; Ohtaka et al., 2001), as illustrated in

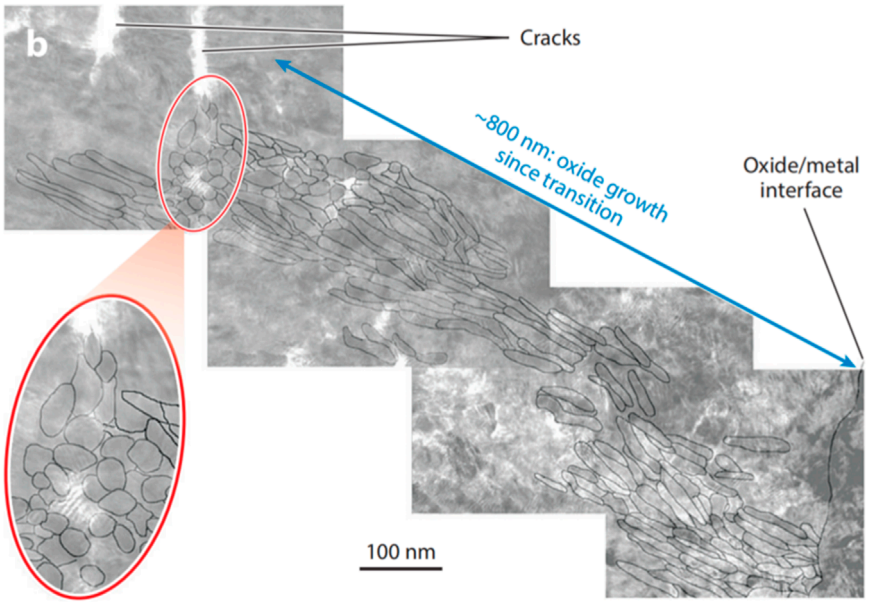

FIGURE 3
Cross-sectional electron micrograph showing columnar and equiaxed oxide grain present in the oxide layer at the time of transition (de Gabory et al., 2015a).

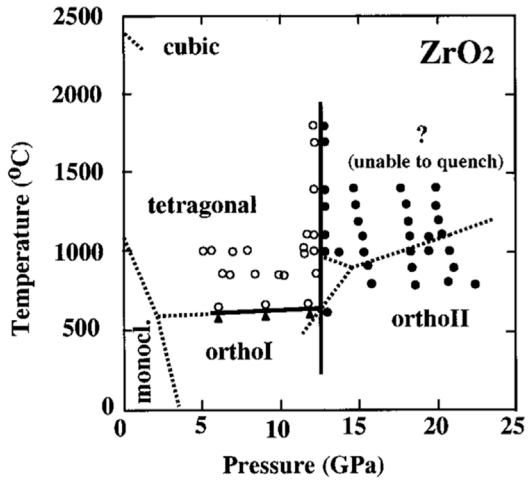

FIGURE 4
Pressure-temperature phase diagram of ZrO_2 (Ohtaka et al., 2001). Reported boundaries are given by dashed lines: monoclinic-to-orthoI and orthoI-to-tetragonal are after Block et al. (1985); monoclinic-to-tetragonal is after Witney (Whitney, 1965); orthoI-to-orthoII and orthoII-to-? is after Ohtaka et al. (1988); Ohtaka et al. (1990); Ohtaka et al. (1991).

Figure 4. Despite t-ZrO_2 being thermodynamically unstable at room temperature or even at the reactor core temperature, it is still observed alongside the monoclinic phase (m-ZrO_2) (Godlewski et al., 1991; Yilmazbayhan et al., 2006). Generally, it is suggested that t-ZrO_2 can be stabilized by the following factors.

3.1.1 Compressive stress

The compressive stress in the oxide film has been extensively investigated by synchrotron X-ray diffraction (S-XRD) (Garvie, 1952; QIN et al., 2007; Sawabe et al., 2015). Sawabe et al. (2015) measured the residual stress using micro-beam XRD and found that the maximum compressive stress is 3.9 GPa at the O-M interface. This stress is attributed to the volume expansion caused by oxidation (Pilling-Bedworth ratio is 1.56) (Polatidis et al., 2013), and gradually decreases further from the O-M interface. Additionally, Qin et al. (2006) and Garvie (1978) reported the coexistence of compressive stress and t-ZrO_2. Kurpaska et al. (2013) observed an increase of t-ZrO_2 fraction with increasing compressive stress using *in situ* Raman spectroscopy, revealing that compressive stress can stabilize t-ZrO_2.

3.1.2 Grain size

Regarding the grain size, Garvie, (1952) and Holmes et al. (1972) suggested that the existence of tetragonal zirconia at a temperature well below the normal transformation temperature can be explained by crystallite size, where surface free energy of t-ZrO_2 is less than that of m-ZrO_2. The thermodynamic model proposed by Qin et al. (2006), as shown in Figure 5, provides an intuitive understanding. It indicates that the t-m transition occurs if the grain size exceeds the critical value, which is sensitive to temperature (Holmes et al., 1972). It is worth noting that there is a disagreement regarding the critical size of t-m transformation, varying from 30 nm (Garvie, 1952) to 90 nm (Garvie et al., 1975).

3.1.3 Vacancies

Fabris et al. (2002) used a self-consistent tight-binding model to calculate energy and structure of zirconia with various vacancy concentrations. They found large relaxations around an oxygen

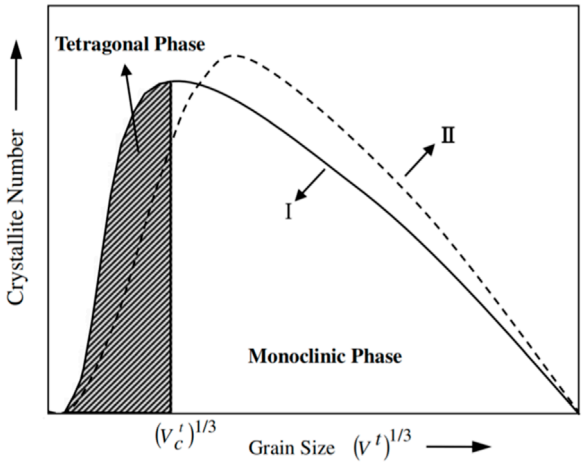

FIGURE 5
A schematic diagram showing two different grain-size distributions of ZrO_2 (I and II), V_C^t is the critical value of the t-m transformation (Qin et al., 2006).

vacancy and vacancy clusters along the <111> direction. Their finding indicated that doped vacancies favor the stability of t-ZrO_2. Shukla and Seal, (2005) reviewed the mechanisms of tetragonal phase stabilization in nanocrystalline, submicrometer-sized, and bulk zirconia. Their comparison suggested that excess oxygen ion vacancies within the ZrO_2 are primarily responsible for the room temperature tetragonal phase stabilization when the grain size is below a critical threshold.

3.1.4 Chemical dopants

At room temperature, Li et al. (1994) and Ghigna et al. (1999) found that t-ZrO_2 can be stabilized by adding cations with a valence of +3. The chemical bond between the dopant cationic and O^{2-} differs significantly from the chemical bond between Zr^{4+} and O^{2-}, resulting in lattice distortion. The size of cation also determines the favorable position of O^{2-} and thus identifies the structure of the lattice (Ghigna et al., 1999).

In summary, according to the discussions above, a conclusion on t-m transformation can be drawn. Initially, the t-ZrO_2 formed at the O-M interface is stabilized by both compressive stress and a small grain size. However, as the oxide grain grows (Qin et al., 2006), and relaxed compressive stress (Polatidis et al., 2013) brought by the oxide further away from the O-M interface, t-ZrO_2 becomes unstable and transforms to m-ZrO_2. The t-m transformation involves 3%–7% volume expansion and 16%–18% shear strain (Platt et al., 2014), potentially leading to the microcracks along grain boundaries (Kelly and Francis Rose, 2002; Chevalier et al., 2009), which may compromise the protective property of oxide film. Therefore, many researchers consider the t-m transformation as the cause of corrosion transition (Godlewski, 1994; Polatidis et al., 2013; Garner et al., 2015; Barberis, 2022; Maroto et al., 2022). However, there is still controversy about this opinion. Yilmazbayhan et al. (2004) observed a higher corrosion rate in a sample with higher fraction of t-ZrO_2, while the Petigny et al. (2000) reached a contrasting conclusion. In addition, Barberis, (2022) reported no abrupt change in t-ZrO_2 fraction before and after the transition. Hence, further investigation is still required to understand the mechanism of the breakaway phenomenon. It is also noticeable that no clear relationship has been established between oxide grain morphology and the lattice structure of ZrO_2.

3.2 Porosity and cracks in the oxidation film

The stress relaxation in oxide film caused by t-m transformation is the common reason for porosity (Qin et al., 2006; Park et al., 2010). The first compelling evidence of the porosity along the oxidation direction in oxide film corroded at 360°C was provided by Hudson et al. (2009), Hudson and Smith (2009), Ni et al. (2010), Ni et al. (2011a), Ni et al. (2011b), Ni et al. (2012) using Fresnel contrast of transmission electron microscopy (TEM), as shown in Figure 6A. Based on the observed porosity, they proposed a corrosion transition mechanism that these nanopores serve as a short path for oxygen diffusion, contributing to breakaway phenomenon. This mechanism was confirmed by their experiments using ^{18}O to trace the diffusion of oxygen and characterization with Nano secondary ion mass spectrometry (NanoSIMS) (Ni et al., 2012). At higher temperature, Cui et al. (2024) observed nanovoids in an oxide film formed at 1,000°C, as depicted in Figure 6B, and attributed their formation of Zr_5Sn_3, secondary phase particles. At the same temperature, Park et al. (2010) observed micro-pores and micro-cracks at oxide grain boundaries as the grain size increases, as shown in Figure 6C. They indicated that these micro-pores and micro-cracks not only enhance oxygen diffusion but also increase the magnitude of local stress, leading to the propagation of cracks.

Cracks serve as another indicator for the degradation of oxide film. Regarding the direction of cracks relative to the O-M interface, they can be classified into two types: lateral cracks along the interface and the vertical cracks perpendicular to the interface. Isolated lateral cracks with relatively small size are frequently observed above the convex part of the O-M interface (Bossis et al., 2000; Ni et al., 2011a; Tejland and Andren, 2012), as shown in Figure 7A. For continuous lateral cracks, they are periodic separated in the oxide film (Yilmazbayhan et al., 2004), as shown in Figure 7B. Based on the oxide film thickness beneath the continuous lateral cracks, it is considered as the symbol of the onset of transition (Yilmazbayhan et al., 2006; Polatidis et al., 2013; Lee et al., 2017). The connection of small lateral cracks is believed to create the continuous ones (Wallwork et al., 1965; Ni et al., 2011a). The compressive stress in the oxide film, which may block the propagation of cracks, can be overcome as the toughened ceramic (Ni et al., 2011a). In contrast, Kim et al. (2011) suggested that the accumulation of hydrogen, caused by the reduction of α-Zr(O) grain boundaries, is responsible for the formation of lateral cracks, based on their experimental observation at 1,000°C. Even though the cracks severely degrade the protective function of oxide film, the exact impact of lateral cracks on the corrosion is disputed. For example, Lee et al. (2017) suggested that the continuous lateral cracks disturb the oxygen diffusion towards the matrix before transition, while no longer having influence on corrosion after transition.

Particular attention is paid to the vertical cracks, as they act as a direct diffusion path for corrosion medium to reach the matrix.

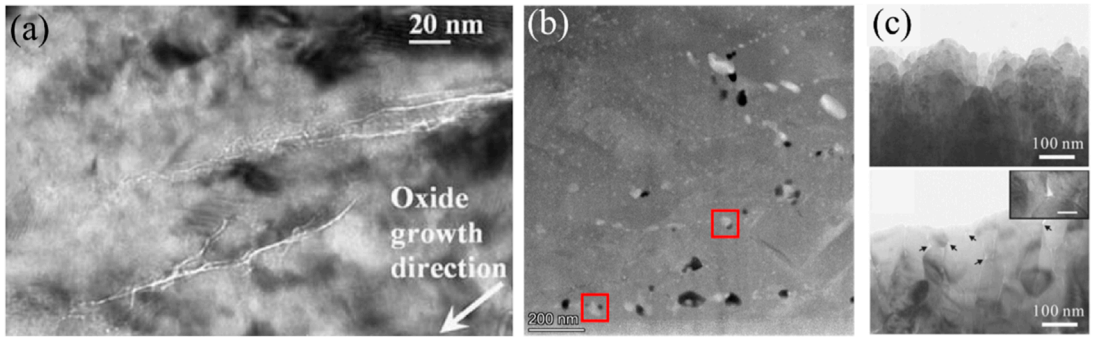

FIGURE 6
The porosity formed in oxide film **(A)** Bright-field Fresnel image of porosity in columnar monoclinic oxide grains formed on Zr-2 alloy at 360°C (Ni et al., 2010); **(B)** Nanovoids formed in oxide of ZIRLO at 1,000°C (Cui et al., 2024); **(C)** Cross-sectional bright-field TEM micrograph obtained from the oxide layer formed on Zr-4 alloy at 1,000°C, the upper one shows the oxide microstructure oxidized for 300 s, the bottom one is obtained after 4,000 s (Park et al., 2010).

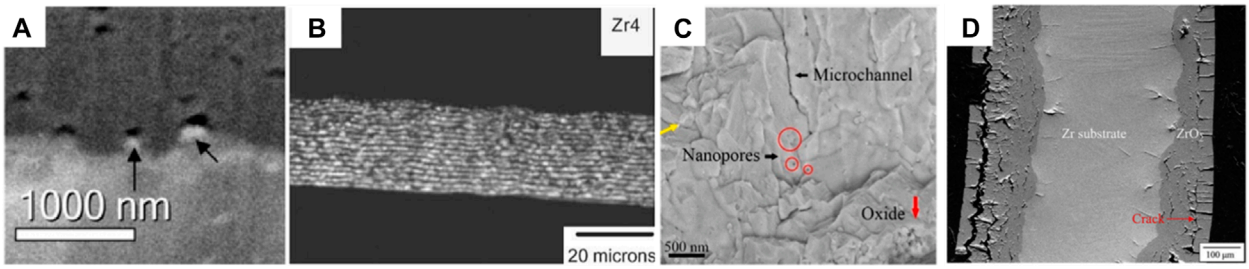

FIGURE 7
(A) The isolated cracks above the O-M interface observed in ZIRLO corroded at 360°C (Ni et al., 2011a); **(B)** The periodic lateral cracks formed in Zr-4 alloy at 360°C (Yilmazbayhan et al., 2004) **(C)** The microchannels above the convex part of O-M interface formed in the oxide film at 1,000°C (Cui et al., 2022); **(D)** SEM BSE imagine of Zr-1Nb0.1Sn0.1Fe pre-oxided at 1,000°C for 1,630 s and subsequently oxidized at 1,000°C for 5,130 s (Lee et al., 2019).

Finite element simulation by Platt et al. (2014) demonstrated that the stress induced by t-m transformation can lead to the formation of cracks along grain boundaries. Clear evidence for continuous nano-pipes along the corrosion direction in the oxide film was provided by Hu et al. (2019) in the corrosion experiment of Zr-0.5Nb, Zr-1Nb and Zr-4 alloy at 360°C. They suggested that these nano-pipes, derived from the connection of nano-pores near the interface, can accelerate the diffusion of hydrogen. Similarly, Figure 7C shows the microchannels perpendicular to the O-M interface (Cui et al., 2022) in an oxide formed at 1,000°C. Cui et al. (2022) believed that these microchannels, located above the concave part of the interface, also result from the connection of nano-pores. At the outer side of oxide film, the tensile stress generated from the convex geometry of the tube leads to vertical cracks starting from the surface of oxide film and propagating toward metal (Lee et al., 2019; Cui et al., 2022). In the matrix adjacent to the O-M interface, Huang et al. (2015) found the vertical cracks next to the aligned β-Nb particles in the corrosion of Zr-0.93Sn-0.82Nb-0.17Fe-0.019S alloy at 360°C. They suggested that the stress concentration caused by delayed oxidation of β-Nb particles is the dominant reason for their formation. At 1,000°C, Lee et al. (2019) also observed vertical cracks in the metal matrix, as shown in Figure 7D, and attribute their formation to the brittle matrix with the concentration of oxygen. During sample preparation, external stress brought from cutting or thermal mounting can easily lead to brittle failure.

4 The oxide-metal interface roughness

As the oxidation progresses through the diffusion of oxygen towards the metal, the O-M interface becomes a focal point where oxidation interactions occur, leading to the growth of oxide film.

4.1 The configuration of O-M interface

Numerous experimental results indicate that the O-M interface formed on zirconium alloy is undulated rather than a flat plane. Barberis et al. (1997) and Blank et al. (1992) described it as cauliflower-like structure, where the larger unit of undulation is composed by a range of second undulations with relatively small sizes. Platt et al. (2015a) and Parise et al. (1998) utilized an

egg-box type structure to illustrate the geometry of the O-M interface, simplifying its shape by employing a sinusoidal function in their calculation. This undulated shape is believed to be caused by different local corrosion rate. Ni et al. (2012) used various techniques, including electron energy loss spectroscopy (EELS), atom probe tomography (APT) and NanoSIMS, to characterize the chemistry of O-M interface formed on ZIRLO and Zr-4 alloy corroded at 360°C using primary water chemistry (pure H_2O with addition of 2 ppm by wt. Li and 1,000 ppm by wt. B). They found that ZrO_2 at the advanced corrosion front (the convex part of O-M interface) and ZrO at the concave part, preserved by slower corrosion rate. Scanning electron microscopy (SEM) and TEM observations from Cui et al. (2022) also supported the conclusion that the convex part of the O-M interface formed on zirconium alloy corroded at 1,000°C is derived from the faster corrosion rate due to microchannels perpendicular to the interface.

As a reflection of local corrosion rate, the roughness of the O-M interface is expected to change with corrosion time, as demonstrated by many published works. Ni et al. (2011a), using focused ion beam sectioning, reconstructed the area around the O-M interface formed on stress-relieved ZIRLO alloy corroded at 360°C, showing the interface roughness as a function of corrosion time, consistent with the tendency observed at 1,000°C (Cui et al., 2022). The roughness reaches a maximum around the transition and gradually decrease afterward. A statistics analysis of the O-M interface amplitude formed in A-0%Sn, ZIRLO, and Zr-4 alloy corrosion experiments at 360°C obtained an identical trend (Platt et al., 2015b). They also observed a recovery after the first reduction, probably caused by a second transition. Cui et al. (2022) provided a detailed explanation of interface roughness evolution, suggesting that the relatively smooth O-M interface after transition represents the completed development of microchannels dominating the corrosion rate in the oxide film.

4.2 The influence of O-M interface

The undulated morphology of the O-M interface, caused by local differences in corrosion rate, has a significant influence on the oxide film, particularly on the stress state of oxide film. Both Parise et al. (1998) and Platt et al. (2015a), using finite element analysis, indicated that the direction of the vertical stress component above the convex part of the undulated interface is opposite to the concave part, as shown in Figure 8A. Parise et al. (1998) also reported that the stress value is positively proportional to the amplitude of undulation, as shown in Figure 8B. When the amplitude of the O-M interface reaches a certain level, the tensile stress in oxide above the convex part of interface is large enough to the form isolated cracks, as observed by numerous works (Bossis et al., 2000; Ni et al., 2011a; Tejland and Andren, 2012; Cui et al., 2022). Furthermore, compressive stress can efficiently stabilize t-ZrO_2, as confirmed by Raman spectroscopy (Cui et al., 2022), aligning with the simulation results of Platt et al. (2014). Building on the vacancy field, Cui et al. (2022) also established a crack formation mechanism for the cases with smooth O-M interface, suggesting that the morphology of cracks strongly depends on the configuration of O-M interface.

5 Alloy elements

5.1 Development of zirconium alloys

So far, the development of zirconium alloys has predominately focused on three systems: Zr-Sn alloy, Zr-Nb alloy, and Zr-Sn-Nb alloy. Initially, the Sn element was induced to eliminate the negative effects of nitrogen introduced by the Kroll process, an industrial method for preparing Zr metal. Consequently, the Zr-1 alloy, known as Zr-2.5Sn, has a similar corrosion behavior to Zr forming a spongy structure. The accidental introduction of transition metal elements, such as Cr, Fe and Ni, significantly improved the corrosion resistance, leading to the development of the Zr-2 alloy. However, Ni, which contributed to increased hydride formation, was eventually replaced by Fe to create the Zr-3 alloy. The early developed Zr-3 alloy, with unsatisfying mechanical properties, underwent further modifications and evolve into the Zr-4 alloy. The currently optimized Zr-4 alloy has been developed with precise control of N content and decreased Sn content, forming the original Zr-System.

Russia originally established the Zr-Nb system (Shebaldov et al., 2000), and was further developed by different countries. For example, France produced the M5 alloy (Zhao, 2001), Canada the Zr-2.5Nb alloy (Warr et al., 1996), and Korea the HANA series alloy (Chakravartty et al., 1995). Combining the advantages of Zr-Sn and Zr-Nb alloy systems, the third generation of zirconium alloy, namely, Zr-Sn-Nb, was developed. This includes the ZIRLO alloy in America (Sabol et al., 1989), the E365 alloy in Russia (Nikulina et al., 1996), and the N18 and N36 alloys in China (Aldeen et al., 2022). Table 1 summarizes the zirconium alloys developed by various countries.

5.2 Influence of alloy element

Considering the development of zirconium alloys, several critical alloy elements, including Nb, Sn and Fe, are reviewed, with a specific focus on the second phase particles (SPPs) that they formed. The main reason is that both the formation and the dissolution of SPPs changes the electrochemistry properties of oxide film, which inevitably influences the oxygen ion diffusion in the oxide. Meanwhile, the delayed oxidation and different thermal behavior of SPPs can lead to concentrated stress and generate cracks.

5.2.1 Nb

Compared with Zr-Sn alloy system, Zr-Nb alloys exhibit a superior corrosion resistance (Kiran Kumar and Szpunar, 2011; Jiang et al., 2022), prompting extensive interest in the impact of Nb. The solid solution of Nb in α-Zr, which is around 0.2–0.5 at%, is much larger than Fe and Cr with an extremely solubility (in the range of 100 s of ppm) (Belle and Mallett, 1954; Douglass and Wagner, 1966). Therefore, a series of investigations were conducted aiming for the influence of Nb dissolved in matrix and oxide. X-ray Absorption Near-Edge Structure (XANES) experiments have indicated that the Nb exist as Nb^{2+} and Nb^{3+} close to O-M interface and fully oxidized to Nb^{5+} around the oxide surface (Froideval et al., 2008; Couet et al., 2015; Moorehead et al., 2019), which consist with the simulation results (Otgonbaatar et al., 2014; Couet et al., 2015). To quantitatively evaluate the effect of Nb on zirconium

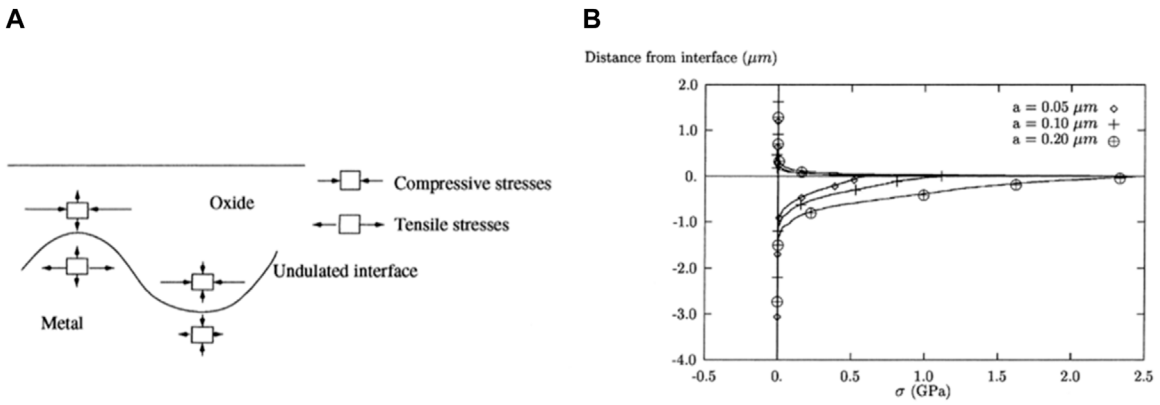

FIGURE 8
The finite element analysis of Parise et al. (1998): **(A)** Schematic distribution of stress around the undulated interface; **(B)** Variation of radial stress (vertical to O-M interface) of an undulated O-M interface with various undulation amplitude and a constant oxide film thickness.

TABLE 1 The alloy component developed by different countries.

Name	Country	Component/wt.%
Zr-1	America	Zr-2.5Sn
Zr-2	America	Zr-1.5Sn-0.15Fe-0.05Ni-0.1Cr
Zr-3	America	Zr-1.5Sn-0.15Fe-0.1Cr
Zr-4	America	Zr-1.5Sn-0.2Fe-0.1Cr
E110	The Soviet Union	Zr-1Nb
M5	France	Zr-1.0Nb-0.16O
Zr-2.5Nb	Canada	Zr-2.5Nb
E635	Russia	Zr-1Nb-1%Sn-0.4Fe
ZIRLO	America	Zr-1.0Sn-1.0Nb-0.1Fe
NDA	Japan	Zr-1.0Sn-1.0Nb-0.4Fe
HANA6	Korea	Zr-1.1Nb-0.05Cu
HANA3	Korea	Zr-1.5Nb-0.4Sn-0.1Fe-0.1Cu
HANA4	Korea	Zr-1.5Nb-0.4Sn-0.2Fe-0.1Cr
N18	China	Zr-1.0Sn-0.1Nb-0.28Fe-0.16Cr-0.01Ni
N36	China	Zr-2.0Sn-1.0Nb-0.3Fe

alloy oxidation, The Coupled Current Charge Compensation (C4) model was established and provided by a good predictions of pre-transition behavior (Couet et al., 2015). The difference in valent between Zr^{4+} and Nb^{3+} creates an effective negative charge of −1 within the oxide film. The negative effective charge can compensate the positive space charge from intrinsic oxygen vacancies and, thus, reduce the positive potential which drives the migration of oxygen vacancy.

In addition, the large number of discrete Nb SPPs also attract the attention of researchers. The presence of SPPs containing Nb is attributed to the low terminal solid solution of Nb in α-Zr. Both Jeong et al. (2024) and Kim et al. (2008) suggested that Nb can completely dissolve in Zr when its concentration is less than 0.29 wt.%. When it exceeds 0.49 wt.%, Nb forms spherical β-Nb particles discretely distributed in the oxide film with a diameter around 50–80 nm (Mardon et al., 2000; Kim et al., 2009a; Jung et al., 2009), shown in Figure 9A. From the electrochemical perspective, the nobler SPPs serve as the cathodic site of micro galvanic corrosion (Weidinger et al., 1991), resulting in the preferential oxidation of the larger area Zr matrix (de Gabory et al., 2015b; Setiadinata, 2016). The calculation of Gibbson free energy (Liu et al., 2023) supported this conclusion, and this phenomenon is referred to as delayed oxidation. After included by oxide film, an amorphization process takes place for the oxidation of β-Nb (Yilmazbayhan et al., 2006; Kim et al., 2009b). Park et al. (2009) suggested that β-Nb particles have a positive effect on corrosion resistance. The discrete β-Nb particles can release the stress caused by the t-m transformation, thus stabilizing the columnar oxide grains. Even though the oxidation of Nb induces stress from volume expansion and local amorphous regions (Kim et al., 2009b), their uniformed distribution benefits the stabilization of stress state in oxide film. Conversely, the negative effect of β-Nb particles on corrosion behavior also stems from their oxidation. The oxidation of β-Nb leads to the formation of Nb_2O_5 (Lin and Woo, 2000), accompanying a large volume expansion with a P-B ratio of 2.67 (Proff et al., 2013). Huang et al. (2015) found cracks along the aligned direction of β-Nb in oxide film, as shown in Figure 9B. They believed that the delayed oxidation of β-Nb leads to the stress concentration with a symbol of Moiré fringes (pronounced mwa-ray pattern in TEM image), and thus produce the cracks.

When the component of Nb is in the range of 0.29–0.49 wt.%, Nb exists as $Zr(Nb,Fe)_2$ with a size on the order of 100 nm (Mardon et al., 2000). Its formation is due to Nb replacing Fe in $ZrFe_3$, which will be discussed in the section of Fe. Generally, the component of Nb in commercial zirconium

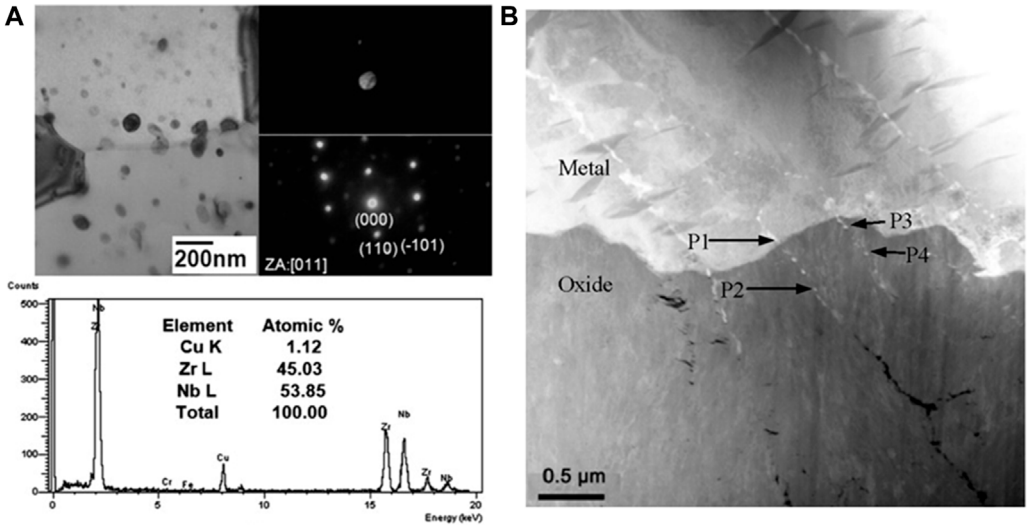

FIGURE 9
(A) Precipitate analysis of the Zr-1.1Nb-0.05Cu alloy after 4h-annealing at 570°C and a final annealing for 8 h at 470°C obtained by Kim et al. (2009a); **(B)** The crack morphology in oxide formed on Zr-0.93Sn-0.82Nb-0.17Fe-0.019S alloy at 360°C (Huang et al., 2015).

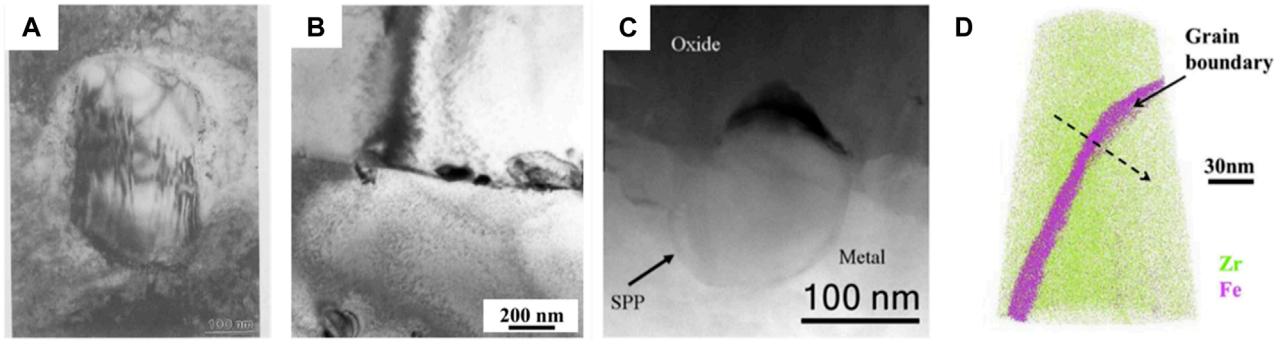

FIGURE 10
(A) Zr (Fe, $Cr)_2$ formed in the matrix after corrosion (Iltis et al., 1995); **(B)** Intergranular Zr (Fe, $Nb)_2$ in Zr-0.99Sn-0.51Fe-1.03Nb observed by Doriot et al. (2005); **(C)** The cracks related to the Zr (Fe, Nb, $Cr)_2$ observed at the O-M interface of ZIRLO at 360°C (Ni et al., 2011a); **(D)** Segregation of Fe at grain boundary in Zr bar after the corrosion experiments at 360°C (Dong et al., 2013).

alloys is controlled around 1wt.%, representing the optimized proportion when taking creep and corrosion resistance in to account simultaneously.

5.2.2 Fe

Fe was induced into zirconium alloys accidently as impurities during smelting process. However, it improved the corrosion resistance surprisingly. In the early stage of investigation, the influence of Fe on corrosion resistance is primarily analyzed through the SPPs. The Zr-Fe phase diagram (Stein et al., 2002) encompasses three structural forms: $ZrFe_2$ (cubic or hexagonal), Zr_2Fe (tetragonal or face-centred cubic structure), and Zr_3Fe (orthorhombic). The addition of other alloying elements, such as Cr and Nb, introduces ternary intermetallic phases. In Figure 10A, the Zr (Fe, $Cr)_2$ is shown, resulting from the replacement of Fe due to the similarity in atomic radii between Fe and Cr (Garzarolli et al., 1996). When a zirconium alloy contains both Fe and Nb simultaneously, the situation is much more complex. Given the similarity in atomic mass (Fe = 56amu, Nb = 93amu, Zr = 91amu) and radii (Fe = 1.3Å, Nb = 1.5Å, Zr = 1.6Å), it is anticipated that Nb can substitute the Zr atoms in Zr-Fe intermetallic phase, as identified in early research of Kanematsu (Kanematsu, 1969). Surprisingly, most reports on ternary ZrNbFe phases state that Nb replaces the Fe rather than Zr, forming Zr $(Fe,Nb)_2$, which is termed as Laves phase, as shown in Figure 10B. However, in reality, ternary ZrNbFe phases are quiet complicated, including at least Zr (Fe, $Nb)_2$, (Zr, $Nb)_2$Fe, and (Zr, $Nb)_3$Fe. According the review of Harte et al. (2018), the clear definition of hexagonal Zr(Fe, $Nb)_2$ and cubic (Zr, $Nb)_2$Fe arises from their separate constituent compositions. As for other phase, there is still an ambiguity in the identification. However, Nb is expected to act as substitutional solutes compared with Fe, since Nb is more similar to Zr. Kim et al. (2005) conducted a series of corrosion experiments using alloys with varying Nb/Fe ratios, indicating that a lower Nb/Fe ratio leads

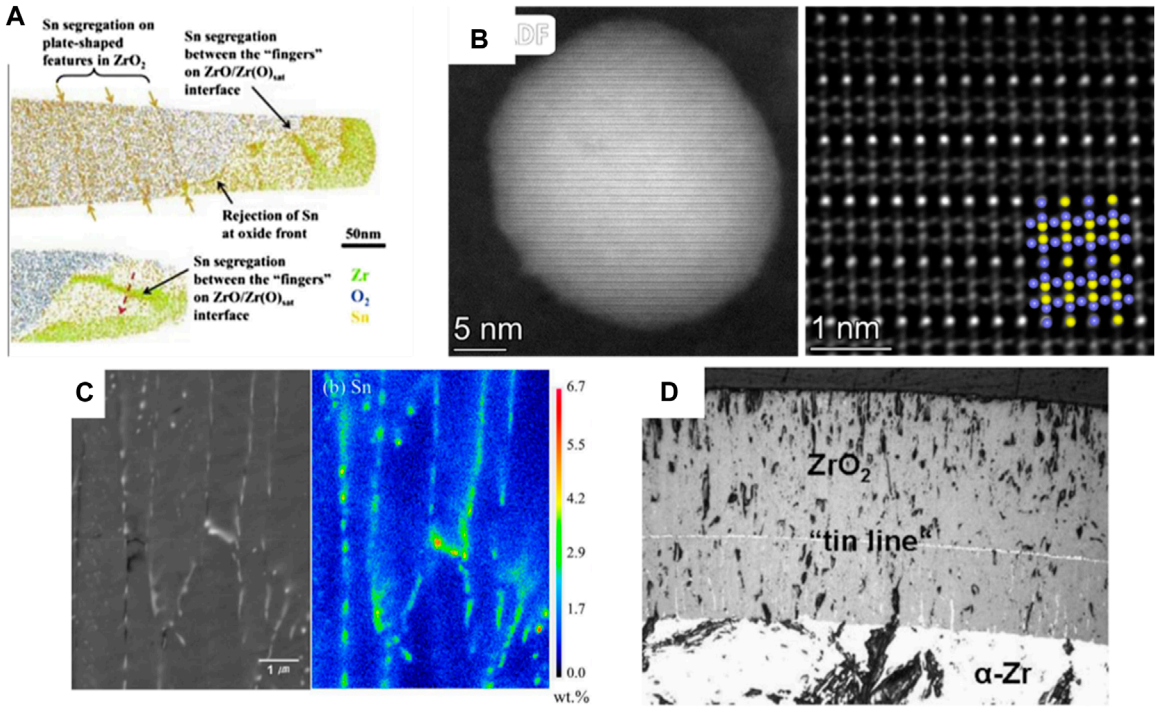

FIGURE 11
The segregation of Sn observed at different temperature **(A)** ATP results of Zr-4 oxidized at 360°C the observed by Dong et al. (2013); **(B)** The atomic arrangement of Zr_5Sn_3 in oxide of ZIRLO formed at 1,000°C from the TEM results of Cui et al. (2024); **(C)** SEM and WDS elemental mapping results of Zr-1Nb-1Sn-0.1Fe oxidized at 1,200°C for 400 s obtained by Lee and Sohn (Lee and Sohn, 2017); **(D)** The tin line formed at 1,400°C observed at the Zry-4 surface by Grosse and Simon (Grosse and Simon, 2009).

to the dominant formation of fcc-$(Zr, Nb)_2Fe$, while the higher Nb/Fe ratio results in mainly formed hcp-$Zr(Fe, Nb)_2$. Due to the complexity and ambiguity of these intermetallic phases, the term Zr-Fe ternary intermetallic phase is used to describe these precipitations.

There is ongoing disagreement regarding the dependence of corrosion resistance on the ternary intermetallic phase containing Zr and Fe. Early investigations using Zr-2 alloy focused on the Zr $(Fe, Cr)_2$. Bojinov et al. (2005) oberved that specimens with a higher number density of Zr $(Fe, Cr)_2$ exhibited a better resistance, contradicting the conclusion of Garzarolli et al. (1996). Meanwhile, Barberis et al. (2002) observed a compact oxide film on the samples with larger Zr $(Fe, Cr)_2$, which is contrast to the findings of Bojinov et al. (2005). A consensus emerges that when Zr-Fe intermetallic phases are larger enough, their delayed oxidation can lead to isolated cracks at the O-M interface, as observed by Ni et al. (2011a) in Figure 10C. It is noteworthy that the redistribution of Fe during the oxidation of Zr-Fe ternary intermetallic phases in the matrix should also be considered. As a heterovalent substitution, iron ions could alter the conductivity of the oxide film, eventually affecting the corrosion resistance, as suggested by Bojinov et al. (2005). Besides conductivity, the Fe ions could also influence the oxygen vacancies, thereby controlling the proportion of t-ZrO_2 as reported by Iltis et al. (1995). With advancement of characterization techniques, Fe is observed to segregate at the grain boundaries in the matrix after corrosion, as shown in Figure 10D. The effect of this Fe segregation on corrosion resistance need further investigation.

5.2.3 Sn

At the beginning, the addition of Sn was introduced to counteract the influence of N, whose ion will replace O^{2-} and accelerated corrosion by creating additional vacancies. The solubility of Sn in α-Zr is about 1.2 at% at 853K (Arias and Roberti, 1983), which means a complete Zr-Sn solid solution is formed in low Sn alloy. It is widely believed that an increasing Sn component could increase the corrosion rate of zirconium alloy (Garde et al., 1994; Steinbrueck and Boettcher, 2011; Wei et al., 2013; Vandegrift et al., 2019). Both Wei et al. (2013) and Garner et al. (2015) observed an increased fraction of t-ZrO_2 with a rising Sn component. It is postulated that Sn^{2+} substitutes for Zr^{4+}, causing the production of vacancies to balance overall charge (Hulme et al., 2016). Therefore, the addition of Sn allows the grain size of t-ZrO_2 to exceed the critical size, as observed by Wei et al. (2013). The further oxidation of Sn^{2+} to Sn^{4+} would contribute to destabilization of tetragonal phase. Meanwhile, the increasing fraction of t-ZrO_2 also implies an increase in t-m transformation, which may result in increased porosity, leading to degradation of the protective oxide film.

In contrast to Nb and Fe, the segregation of Sn was observed in the oxide film rather than metal matrix at both operation condition and higher temperatures. The only experimental evidence for Sn

segregation at service condition (360°C), as shown in Figure 11A, is from ATP by Dong et al. (2013) in oxide formed at 360°C. The density functional theory (DFT) simulation by Yuan et al. (2021) also confirmed Sn segregation at service conditions. At 1,000°C, TEM by Cui et al. (2024) found the Zr-Sn intermetallic phase, Zr_5Sn_3, formed in the oxide film and considered it as the source of nanovoids (Figure 11B). DFT and *ab initio* molecular dynamics (AIMD) simulations showed that Sn atoms in Zr_5Sn_3 tend to diffuse towards ZrO_2, accompanied by a flux of oxygen atoms in the opposite direction. The diffusion is common in the delayed oxidation process of SPPs, where Sn transforms from binding defects, $\{Sn_{Zr}: V_O\}$, to isolated Sn^{4+} (Bell et al., 2018). As a result, the remaining vacancies segregate at the interface between Zr_5Sn_3 and ZrO_2, and form nanovoids aligned along oxide grain boundaries. Lee and Sohn (Lee and Sohn, 2017) found Zr_5Sn_3 and $ZrSn_2$ at grain boundaries of zirconia formed at 1,200°C using SEM and wavelength dispersive spectroscopy (WDS), shown in Figure 11C, and argued that they impede the diffusion of oxygen, thus improving the corrosion resistance. When temperature exceeds 1,300°C, Pawel et al. (1977), Dobson et al. (1977) and Grosse and Simon (Grosse and Simon, 2009) observed Sn segregation parallel to the O-M interface, as depicted in Figure 11D. Pawel et al. (1977) suggested that the oxide film tends to spall along the Sn line. Therefore, it is suggested that Sn segregation on grain boundaries at higher temperature can increase the corrosion rate.

6 Summary and prospect

The present work reviewed the corrosion kinetics, microstructural evolution of oxide film, the O-M interface, and the influence of alloy elements. The key findings and prospects are outlined as follows:

(1) Sudden accelerations in corrosion, commonly called the "breakaway" phenomenon, is observed at either high temperature or low temperature. Two widely accepted mechanisms are proposed: t-m transformation and porosity permit short paths for oxygen diffusion. Although the latter is observed under both normal operation conditions and accident conditions, further investigations are required to determine if a unified mechanism operates at different temperatures.

(2) The stress of oxide plays an important role in oxidation behavior. Since for zirconium alloy, it not only affects the diffusion coefficient directly, but also determine the t-m transformation. Apart from volume expansion caused by oxidation, the geometry of tube and undulated O-M interface also act as internal stress source. A quantitative investigation should is needed to identify the accurate influence of these factors.

(3) Extensive research on the influence of alloying elements has been conducted based on SPPs, or lack thereof. However, accurate identification is challenging due to their small size and complex composition. Contradictions in the impact of alloying components exist, highlighting the need for a more universal mechanism to explain the effects of various alloying elements.

Author contributions

YT: Writing–review and editing, Writing–original draft, Methodology, Investigation, Formal Analysis, Conceptualization. JL: Writing–review and editing, Writing–original draft, Resources, Funding acquisition, Formal Analysis. DY: Writing–review and editing, Writing–original draft, Supervision, Methodology, Formal Analysis.

Funding

The author(s) declare that financial support was received for the research, authorship, and/or publication of this article. This work was supported by the National Natural Science Foundation of China (No. 52101104) and Natural Science Foundation of Sichuan Province (No. 2023NSFSC0409).

Conflict of interest

The authors declare that the research was conducted in the absence of any commercial or financial relationships that could be construed as a potential conflict of interest.

Publisher's note

References

Aldeen, A. W., Chen, Z. W., Disher, I. A., Zhu, Y., and Yan, K. (2022). Growth kinetics of second phase particles in N36 zirconium alloy: Zr–Sn–Nb–Fe. *J. Mater. Res. Technol.* 17, 2038–2046. doi:10.1016/j.jmrt.2022.01.142

Allen, T.R., Konings, R.J.M., and Motta, A.T. (2012a). 5.03 corrosion of zirconium alloys. *Comprehensive Nuclear Materials* 5, 49–68.

Allen, T. R., Konings, R. J. M., and Motta, A. T. (2012b). *Corrosion of zirconium alloys*. Amsterdam, The Netherlands: Elsevier Inc. doi:10.1016/B978-0-08-056033-5.00063-X

Arias, D., and Roberti, L. (1983). The solubility of tin in α and β zirconium below 1000°C. *J. Nucl. Mater.* 118, 143–149. doi:10.1016/0022-3115(83)90219-2

Arima, T., Miyata, K., Inagaki, Y., and Idemitsu, K. (2004). Oxidation properties of Zr–Nb alloys at 500–600°C under low oxygen potentials. *Corros. Sci.* 47, 435–446. doi:10.1016/j.corsci.2004.06.011

Baek, J. H., and Jeong, Y. H. (2008). Breakaway phenomenon of Zr-based alloys during a high-temperature oxidation. *J. Nucl. Mater.* 372, 152–159. doi:10.1016/j.jnucmat.2007.02.011

Barberis, P. (2022). Zirconia powders and Zircaloy oxide films: tetragonal phase evolution during 400°C autoclave tests. *J. Nucl. Mater.* 226, 34–43. doi:10.1016/0022-3115(95)00108-5

Barberis, P., Ahlberg, E., Simic, N., Charquet, D., Lemaignan, C., Wikmark, G., et al. (2002). "Role of the second-phase particles in zirconium binary alloys, in. Zirconium in the Nuclear Industry: Thirteenth International Symposium, ASTM International, 100 Barr Harbor Drive, PO Box C700," West Conshohocken, PA 19428-2959, 33–58. doi:10.1520/STP11382S

Barberis, P., MerleMejean, T., and Quintard, P. (1997). On Raman spectroscopy of zirconium oxide films. *J. Nucl. Mater.* 246, 232–243. doi:10.1016/s0022-3115(97)00038-x

Bell, B. D. C., Murphy, S. T., Grimes, R. W., and Wenman, M. R. (2018). The effect of Sn–VO defect clustering on Zr alloy corrosion. *Corros. Sci.* 141, 14–17. doi:10.1016/j.corsci.2018.06.020

Belle, J., and Mallett, M. W. (1954). Kinetics of the high temperature oxidation of zirconium. *J. Electrochem Soc.* 101, 339. doi:10.1149/1.2781278

Blank, H., Bart, G., and Thiele, H. (1992). Structural-analysis of oxide scales grown on zirconium alloys in autoclaves and in A PWR. *J. Nucl. Mater.* 188, 273–279. doi:10.1016/0022-3115(92)90484-3

Block, S., Da Jornada, J. A. H., and Piermarini, G. J. (1985). Pressure-temperature phase diagram of zirconia. *J. Am. Ceram. Soc.* 68, 497–499. doi:10.1111/j.1151-2916.1985.tb15817.x

Bojinov, M., Hansson-Lyyra, L., Kinnunen, P., Saario, T., and Sirkiä, P. (2005). "*In-situ* studies of the oxide film properties on BWR fuel cladding materials," in Zirconium in the Nuclear Industry: Fourteenth International Symposium, ASTM International, 100 Barr Harbor Drive, PO Box C700, West Conshohocken, PA, 367–385. doi:10.1520/STP37516S

Bossis, P., Lelièvre, G., Barberis, P., Iltis, X., and Lefebvre, F. (2000). "Multi-Scale characterization of the metal-oxide interface of zirconium alloys," in Zirconium in the Nuclear Industry: Twelfth International Symposium, ASTM International, 100 Barr Harbor Drive, PO Box C700, West Conshohocken, PA, 918–945. 19428-2959. doi:10.1520/STP14334S

Chakravartty, J. K., Dey, G. K., Banerjee, S., and Prasad, Y. V. R. K. (1995). Characterization of hot deformation behaviour of Zr-2.5Nb-0.5Cu using processing maps. *J. Nucl. Mater.* 218, 247–255. doi:10.1016/0022-3115(94)00379-3

Charquet, D. (2001). Influence of precipitate density on the nodular corrosion resistance of Zr–Sn–Fe–Cr alloys at 500°C. *J. Nucl. Mater.* 288, 237–240. doi:10.1016/S0022-3115(00)00728-5

Chevalier, J., Gremillard, L., Virkar, A. V., and Clarke, D. R. (2009). The tetragonal-monoclinic transformation in zirconia: lessons learned and future trends. *J. Am. Ceram. Soc.* 92, 1901–1920. doi:10.1111/j.1551-2916.2009.03278.x

Couet, A., Motta, A. T., and Ambard, A. (2015). The coupled current charge compensation model for zirconium alloy fuel cladding oxidation: I. Parabolic oxidation of zirconium alloys. *Parabolic Oxid. zirconium alloys* 100, 73–84. doi:10.1016/j.corsci.2015.07.003

Cox, B. (2005). Some thoughts on the mechanisms of in-reactor corrosion of zirconium alloys. *J. Nucl. Mater.* 336, 331–368. doi:10.1016/j.jnucmat.2004.09.029

Cox, B., and Pemsler, J. P. (1968). Diffusion of oxygen in growing zirconia films. *J. Nucl. Mater.* 28, 73–78. doi:10.1016/0022-3115(68)90058-5

Cui, Z., Liu, J., Hu, P., Qiu, J., Xie, S., Meng, R., et al. (2022). Role of microchannels in breakaway oxidation of Zr alloy under high-temperature steam oxidation at 1000 °C. *Corros. Sci.* 199, 110204. doi:10.1016/j.corsci.2022.110204

Cui, Z., Liu, J., Liu, G., Tang, G., Liu, X., Meng, R., et al. (2024). Understanding the oxidation resistance of zirconium alloy at 1000°C based on the formation of a Zr-Sn intermetallic phase and co-precipitation of Sn and Nb. *Acta Mater* 265, 119622. doi:10.1016/j.actamat.2023.119622

de Gabory, B., Dong, Y., Motta, A. T., and Marquis, E. A. (2015b). EELS and atom probe tomography study of the evolution of the metal/oxide interface during zirconium alloy oxidation. *J. Nucl. Mater.* 462, 304–309. doi:10.1016/j.jnucmat.2015.03.043

de Gabory, B., Motta, A. T., and Wang, K. (2015a). Transmission electron microscopy characterization of Zircaloy-4 and ZIRLO™ oxide layers. *J. Nucl. Mater.* 456, 272–280. doi:10.1016/j.jnucmat.2014.09.073

Dobson, W. G., Biederman, R. R., and Ballinger, R. G. (1977). "Zircaloy-4 oxidation in steam under transient oxidizing conditions," in *Zirconium in the nuclear industry* (United States: ASTM International).

Dong, Y., Motta, A. T., and Marquis, E. A. (2013). Atom probe tomography study of alloying element distributions in Zr alloys and their oxides. *J. Nucl. Mater.* 442, 270–281. doi:10.1016/j.jnucmat.2013.08.055

Doriot, S., Gilbon, D., Béchade, J.-L., Mathon, M.-H., Legras, L., and Mardon, J.-P. (2005). "Microstructural stability of M5™ alloy irradiated up to high neutron fluences," in Zirconium in the Nuclear Industry: Fourteenth International Symposium, ASTM International, 100 Barr Harbor Drive, PO Box C700, West Conshohocken, PA, 175–201. 19428-2959. doi:10.1520/STP37507S

Douglass, D. L., and Wagner, C. (1966). The oxidation of oxygen-deficient zirconia and its relationship to the oxidation of zirconium. *J. Electrochem Soc.* 113, 671. doi:10.1149/1.2424088

Fabris, S., Paxton, A. T., and Finnis, M. W. (2002). A stabilization mechanism of zirconia based on oxygen vacancies only. *Acta Mater* 50, 5171–5178. doi:10.1016/S1359-6454(02)00385-3

Froideval, A., Degueldre, C., Segre, C. U., Pouchon, M. A., and Grolimund, D. (2008). Niobium speciation at the metal/oxide interface of corroded niobium-doped Zircaloys: a X-ray absorption near-edge structure study. *Corros. Sci.* 50, 1313–1320. doi:10.1016/j.corsci.2008.01.011

Garde, A. M., Pati, S. R., Krammen, M. A., Smith, G. P., and Endter, R. K. (1994). *Corrosion behavior of Zircaloy-4 cladding with varying tin content in high-temperature pressurized water reactors*. Philadelphia, PA (United States): ASTM.

Garner, A., Hu, J., Harte, A., Frankel, P., Grovenor, C., Lozano-Perez, S., et al. (2015). The effect of Sn concentration on oxide texture and microstructure formation in zirconium alloys. *Acta Mater.* 99, 259–272. doi:10.1016/j.actamat.2015.08.005

Garvie, R. C. (1952). Stabilization of the tetragonal structure in zirconia microcrystals. *J. Phys. Chem.* 82 (1978), 218–224. doi:10.1021/j100491a016

Garvie, R. C. (1978). Stabilization of the tetragonal structure in zirconia microcrystals. *J. Phys. Chem.* 82, 218–224. doi:10.1021/j100491a016

Garvie, R. C., Hannink, R. H., and Pascoe, R. T. (1975). Ceramic steel? *Nature* 258, 703–704. doi:10.1038/258703a0

Garzarolli, F., Stehle, H., and Steinberg, E. (1996). "Behavior and properties of zircaloys in power reactors: a short review of pertinent aspects in lwr fuel," in Zirconium in the Nuclear Industry: Eleventh International Symposium, ASTM International, 100 Barr Harbor Drive, PO Box C700, West Conshohocken, PA, 12–32. doi:10.1520/STP16165S

Ghigna, P., Spinolo, G., Anselmi-Tamburini, U., Maglia, F., Dapiaggi, M., Spina, G., et al. (1999). Fe-doped zirconium oxide produced by self-sustained high-temperature synthesis: evidence for an Fe–Zr direct bond. *J. Am. Chem. Soc.* 121, 301–307. doi:10.1021/ja982335a

Godlewski, J. (1994). *How the tetragonal zirconia is stabilized in the oxide scale that is formed on a zirconium alloy corroded at 400°C in steam*.

Godlewski, J., Gros, J. P., Lambertin, M., Wadier, J. F., and Weidinger, H. (1991). *Raman spectroscopy study of the tetragonal-to-monoclinic transition in zirconium oxide scales and determination of overall oxygen diffusion by nuclear microanalysis of O*. West Conshohocken, PA: ASTM Special Technical Publication, 416–434.

Grosse, M., and Simon, R. (2009). Analysis of tin diffusion in Zircaloy-4 and tin redistribution after steam oxidation by means of X-ray fluorescence measurements. *Adv. Eng. Mater* 11, 483–487. doi:10.1002/adem.200800344

Harte, A., Griffiths, M., and Preuss, M. (2018). The characterisation of second phases in the Zr-Nb and Zr-Nb-Sn-Fe alloys: a critical review. *J. Nucl. Mater.* 505, 227–239. doi:10.1016/j.jnucmat.2018.03.030

Holmes, H. F., Fuller, E. L., and Gammage, R. B. (1972). Heats of immersion in the zirconium oxide-water system. *J. Phys. Chem.* 76, 1497–1502. doi:10.1021/j100654a023

Hu, J., Liu, J., Lozano-Perez, S., Grovenor, C. R. M., Christensen, M., Wolf, W., et al. (2019). Hydrogen pickup during oxidation in aqueous environments: the role of nano-pores and nano-pipes in zirconium oxide films. *Acta Mater* 180, 105–115. doi:10.1016/j.actamat.2019.09.005

Huang, J., Yao, M., Gao, C., Liang, X., Peng, J., Zhang, J., et al. (2015). The influence of second phase particles on the crack formation in oxide films formed on zirconium alloys. *Corros. Sci.* 99, 172–177. doi:10.1016/j.corsci.2015.06.030

Hudson, D., Ni, N., Lozano-Perez, S., Saxey, D., English, C., Smith, G., et al. (2009). *The atomic scale structure and chemistry of the zircaloy-4 metal-oxide interface*.

Hudson, D., and Smith, G. D. W. (2009). Initial observation of grain boundary solute segregation in a zirconium alloy (ZIRLO) by three-dimensional atom probe. *Scr. Mater* 61, 411–414. doi:10.1016/j.scriptamat.2009.04.032

Hulme, H., Baxter, F., Babu, R. P., Denecke, M. A., Gass, M., Steuwer, A., et al. (2016). An X-ray absorption near-edge structure (XANES) study of the Sn L3 edge in zirconium alloy oxide films formed during autoclave corrosion. *Corros. Sci.* 105, 202–208. doi:10.1016/j.corsci.2016.01.018

Iltis, X., Lefebvre, F., and Lemaignan, C. (1995). Microstructural study of oxide layers formed on Zircaloy-4 in autoclave and in reactor part 11: impact of the chemical evolution of intermetallic precipitates on their zirconia environment. *J. Nucl. Mater.* 224, 121–130. doi:10.1016/0022-3115(95)00069-0

Jeong, Y. H., Baek, B. J., and Park, S. Y. (1999). *Waterside corrosion of zirconium alloys in nuclear power plants*.

Jeong, Y. H., Kim, H. G., and Kim, T. H. (2024). Effect of β phase, precipitate and Nb-concentration in matrix on corrosion and oxide characteristics of Zr–xNb alloys. *J. Nucl. Mater.* 317, 1–12. doi:10.1016/s0022-3115(02)01676-8

Jiang, G., Xu, D., Yang, W., Liu, L., Zhi, Y., and Yang, J. (2022). High-temperature corrosion of Zr–Nb alloy for nuclear structural materials. *Prog. Nucl. Energy* 154, 104490. doi:10.1016/j.pnucene.2022.104490

Jung, Y.-I., Lee, M.-H., Kim, H.-G., Park, J.-Y., and Jeong, Y.-H. (2009). Behavior of a recrystallization in HANA-4 and HANA-6 zirconium-based alloys. *J. Alloys Compd.* 479, 423–426. doi:10.1016/j.jallcom.2008.12.089

Kanematsu, K. (1969). Structural and Magnetic Properties of Pseudobinary System ($Zr_{1-<i>x</i>}Nb_{<i>x</i>}$)$Fe_2$. *J. Phys. Soc. Jpn.* 27, 849–856. doi:10.1143/jpsj.27.849

Kelly, P. M., and Francis Rose, L. R. (2002). The martensitic transformation in ceramics — its role in transformation toughening. *Prog. Mater Sci.* 47, 463–557. doi:10.1016/S0079-6425(00)00005-0

Kim, H.-G., Choi, B.-K., Park, J.-Y., Cho, H.-D., and Jeong, Y.-H. (2009b). Analysis of oxidation behavior of the β-Nb phase formed in Zr–1.5Nb alloy by using the HVEM. *J. Alloys Compd.* 481, 867–871. doi:10.1016/j.jallcom.2009.03.144

Kim, H.-G., Choi, B.-K., Park, J.-Y., and Jeong, Y.-H. (2009a). Influence of the manufacturing processes on the corrosion of Zr-1.1Nb-0.05Cu alloy. *Corros. Sci.* 51, 2400–2405. doi:10.1016/j.corsci.2009.06.023

Kim, H. G., Kim, I. H., Choi, B. K., and Park, J. Y. (2011). A study of the breakaway oxidation behavior of zirconium cladding materials. *J. Nucl. Mater.* 418, 186–197. doi:10.1016/j.jnucmat.2011.06.039

Kim, H.-G., Park, J.-Y., and Jeong, Y.-H. (2005). Ex-reactor corrosion and oxide characteristics of Zr–Nb–Fe alloys with the Nb/Fe ratio. *J. Nucl. Mater.* 345, 1–10. doi:10.1016/j.jnucmat.2005.04.061

Kim, H. G., Park, S. Y., Lee, M. H., Jeong, Y. H., and Kim, S. D. (2008). Corrosion and microstructural characteristics of Zr-Nb alloys with different Nb contents. *J. Nucl. Mater.* 373, 429–432. doi:10.1016/j.jnucmat.2007.05.035

Kiran Kumar, N. A. P., and Szpunar, J. A. (2011). EBSD studies on microstructure and crystallographic orientation of δ-hydrides in Zircaloy-4, Zr–1% Nb and Zr–2.5% Nb. *Mater Sci. Eng. A Struct. Mater* 528, 6366–6374. doi:10.1016/j.msea.2011.05.022

Kurpaska, L., Favergeon, J., Lahoche, L., Moulin, G., El Marssi, M., and Roelandt, J.-M. (2013). Zirconia layer formed by high temperature oxidation of pure zirconium: stress generated at the zirconium/zirconia interface. *Oxid. Metals* 79, 261–277. doi:10.1007/s11085-012-9348-9

Lee, C. M., Kim, G., Sohn, D.-S., Han, Y.-S., and Mok, Y.-K. (2019). Short communication on "self-crack-healing behavior of oxide formed on a zirconium alloy cladding tube,". *J. Nucl. Mater.* 526, 151749. doi:10.1016/j.jnucmat.2019.151749

Lee, C. M., Mok, Y. K., and Sohn, D. S. (2017). High-temperature steam oxidation and oxide crack effects of Zr-1Nb-1Sn-0.1Fe fuel cladding. *J. Nucl. Mater.* 496, 343–352. doi:10.1016/j.jnucmat.2017.10.013

Lee, C. M., and Sohn, D.-S. (2017). Enhanced high-temperature oxidation resistance of a zirconium alloy cladding by high-temperature preformed oxide on the cladding. *Corros. Sci.* 131, 116–125. doi:10.1016/j.corsci.2017.11.019

Leistikow, S., and Schanz, S. G. (2022). The oxidation behavior of Zircaloy-4 in steam between 600 and 1600°C. *Mater. Corros.* 36, 105–116. doi:10.1002/maco.19850360302

Li, P., Chen, I.-W., and Penner-Hahn, J. E. (1994). Effect of dopants on zirconia stabilization-an X-ray absorption study: I, trivalent dopants. *J. Am. Ceram. Soc.* 77, 118–128. doi:10.1111/j.1151-2916.1994.tb06964.x

Lin, Y. P., and Woo, O. T. (2000). Oxidation of β-Zr and related phases in Zr–Nb alloys: an electron microscopy investigation. *J. Nucl. Mater.* 277, 11–27. doi:10.1016/S0022-3115(99)00153-1

Liu, J., Tang, C., Steinbrück, M., Yang, J., Stegmaier, U., Große, M., et al. (2021). Transient experiments on oxidation and degradation of Cr-coated Zircaloy in steam up to 1600 °C. *Corros. Sci.* 192, 1. doi:10.1016/j.corsci.2021.109805

Liu, J., Xie, Y., Hao, Z., Cui, Z., Meng, R., Zhao, F., et al. (2023). Self-toughening mechanism of the ZrO2 scale and the precipitation of Sn during the steam oxidation of ZIRLO™ at 1200 °C. *Acta Mater.* 256, 119114. doi:10.1016/j.actamat.2023.119114

Mardon, J.-P., Charquet, D., and Senevat, J. (2000). "Influence of composition and fabrication process on out-of-pile and in-pile properties of M5 alloy," in Zirconium in the Nuclear Industry: Twelfth International Symposium, ASTM International, 100 Barr Harbor Drive, PO Box C700, West Conshohocken, PA, 505–524. doi:10.1520/STP14314S

Maroto, A. J. G., Bordoni, R., Villegas, M., Olmedo, A. M., Blesa, M. A., Iglesias, A., et al. (2022). Growth and characterization of oxide layers on zirconium alloys. *J. Nucl. Mater.* 229, 79–92. doi:10.1016/0022-3115(95)00233-2

Moorehead, M., Yu, Z., Borrel, L., Hu, J., Cai, Z., and Couet, A. (2019). Comprehensive investigation of the role of Nb on the oxidation kinetics of Zr-Nb alloys. *Corros. Sci.* 155, 173–181. doi:10.1016/j.corsci.2019.04.017

Motta, A. T., Couet, A., and Comstock, R. J. (2015). Corrosion of zirconium alloys used for nuclear fuel cladding. *Annu. Rev. Mater Res.* 45, 311–343. doi:10.1146/annurev-matsci-070214-020951

Nagase, F., Otomo, T., and Uetsuka, H. (2003). Oxidation kinetics of low-Sn zircaloy-4 at the temperature range from 773 to 1,573K. *J. Nucl. Sci. Technol.* 40, 213–219. doi:10.1080/18811248.2003.9715351

Ni, N., Hudson, D., Wei, J., Wang, P., Lozano-Perez, S., Smith, G. D. W., et al. (2012). How the crystallography and nanoscale chemistry of the metal/oxide interface develops during the aqueous oxidation of zirconium cladding alloys. *Acta Mater* 60, 7132–7149. doi:10.1016/j.actamat.2012.09.021

Ni, N., Lozano-Perez, S., Jenkins, M. L., English, C., Smith, G. D. W., Sykes, J. M., et al. (2010). Porosity in oxides on zirconium fuel cladding alloys, and its importance in controlling oxidation rates. *Scr. Mater* 62, 564–567. doi:10.1016/j.scriptamat.2009.12.043

Ni, N., Lozano-Perez, S., Sykes, J., and Grovenor, C. (2011b). Quantitative EELS analysis of zirconium alloy metal/oxide interfaces. *Ultramicroscopy* 111, 123–130. doi:10.1016/j.ultramic.2010.10.020

Ni, N., Lozano-Perez, S., Sykes, J., Smith, G., and Grovenor, C. (2011a). Focussed ion beam sectioning for the 3D characterisation of cracking in oxide scales formed on commercial ZIRLO™ alloys during corrosion in high temperature pressurised water. *Corros. Sci.* 53, 4073–4083. doi:10.1016/j.corsci.2011.08.013

Nikulina, A., Markelov, V., Peregud, M., Bibilashvili, Y., Kotrekhov, V., Lositsky, A., et al. (1996). "Zirconium alloy E635 as a material for fuel rod cladding and other components of VVER and RBMK cores," in Zirconium in the Nuclear Industry: Eleventh International Symposium, ASTM International, 100 Barr Harbor Drive, PO Box C700, West Conshohocken, PA, 785–804. doi:10.1520/STP16201S

Ohtaka, O., Fukui, H., Kunisada, T., Fujisawa, T., Funakoshi, K., Utsumi, W., et al. (2001). Phase relations and equations of state of ZrO 2 under high temperature and high pressure. *Phys. Rev. B* 63, 174108. doi:10.1103/physrevb.63.174108

Ohtaka, O., Kume, S., and Ito, E. (1990). Stability field of cotunnite-type zirconia. *J. Am. Ceram. Soc.* 73, 744–745. doi:10.1111/j.1151-2916.1990.tb06584.x

Ohtaka, O., Kume, S., Iwami, T., and Urabe, K. (1988). Synthesis of the orthorhombic phase of 2Y˙ZrO2. *J. Am. Ceram. Soc.* 71, C-164–C–166. doi:10.1111/j.1151-2916.1988.tb05043.x

Ohtaka, O., Yamanaka, T., Kume, S., Ito, E., and Navrotsky, A. (1991). Stability of monoclinic and orthorhombic zirconia: studies by high-pressure phase equilibria and calorimetry. *J. Am. Ceram. Soc.* 74, 505–509. doi:10.1111/j.1151-2916.1991.tb04051.x

Otgonbaatar, U., Ma, W., Youssef, M., and Yildiz, B. (2014). Effect of niobium on the defect chemistry and oxidation kinetics of tetragonal ZrO 2. *J. Phys. Chem. C* 118, 20122–20131. doi:10.1021/jp504874v

Parise, M., Sicardy, O., and Cailletaud, G. (1998). Modelling of the mechanical behavior of the metal-oxide system during Zr alloy oxidation. *J. Nucl. Mater.* 256, 35–46. doi:10.1016/s0022-3115(98)00045-2

Park, D. J., Park, J. Y., Jeong, Y. H., and Lee, J. Y. (2010). Microstructural characterization of ZrO2 layers formed during the transition to breakaway oxidation. *J. Nucl. Mater.* 399, 208–211. doi:10.1016/j.jnucmat.2010.01.021

Park, J.-Y., Choi, B.-K., Yoo, S. J., and Jeong, Y. H. (2009). "Corrosion and oxide properties of HANA alloys," in Zirconium in the Nuclear Industry: 15th International Symposium.

Park, J.-Y., Yoo, S. J., Choi, B.-K., and Jeong, Y. H. (2007). Oxide microstructures of advanced Zr alloys corroded in 360°C water loop. *J. Alloys Compd.* 437, 274–279. doi:10.1016/j.jallcom.2006.07.101

Pawel, R. E., Perkins, R. A., McKee, R. A., V Cathcart, J., Yurek, G., and Druschel, R. (1977). Diffusion of oxygen in beta-zircaloy and the high temperature zircaloy-steam reaction, Zirconium in the Nuclear Industry. *ASTM STP* 633, 119–133.

Petigny, N., Barberis, P., Lemaignan, C., Valot, C., and Lallemant, M. (2000). *In situ* XRD analysis of the oxide layers formed by oxidation at 743 K on Zircaloy 4 and Zr-1NbO. *J. Nucl. Mater.* 280, 318–330. doi:10.1016/s0022-3115(00)00051-9

Pieraggi, B., Rapp, R. A., and Hirth, J. P. (1995). Role of interface structure and interfacial defects in oxide scale growth. *Oxid. Metals* 44, 63–79. doi:10.1007/BF01046723

Platt, P., Frankel, P., Gass, M., Howells, R., and Preuss, M. (2014). Finite element analysis of the tetragonal to monoclinic phase transformation during oxidation of zirconium alloys. *J. Nucl. Mater.* 454, 290–297. doi:10.1016/j.jnucmat.2014.08.020

Platt, P., Frankel, P., Gass, M., and Preuss, M. (2015a). Critical assessment of finite element analysis applied to metal–oxide interface roughness in oxidising zirconium alloys. *J. Nucl. Mater.* 464, 313–319. doi:10.1016/j.jnucmat.2015.05.002

Platt, P., Wedge, S., Frankel, P., Gass, M., Howells, R., and Preuss, M. (2015b). A study into the impact of interface roughness development on mechanical degradation of oxides formed on zirconium alloys. *J. Nucl. Mater.* 459, 166–174. doi:10.1016/j.jnucmat.2015.01.028

Polatidis, E., Frankel, P., Wei, J., Klaus, M., Comstock, R. J., Ambard, A., et al. (2013). Residual stresses and tetragonal phase fraction characterisation of corrosion tested Zircaloy-4 using energy dispersive synchrotron X-ray diffraction, *J. Nucl. Mater.* 432 102–112. doi:10.1016/j.jnucmat.2012.07.025

Proff, C., Abolhassani, S., and Lemaignan, C. (2013). Oxidation behaviour of zirconium alloys and their precipitates – a mechanistic study. *J. Nucl. Mater.* 432, 222–238. doi:10.1016/j.jnucmat.2012.06.026

Qin, W., Nam, C., Li, H. L., and Szpunar, J. A. (2006). Tetragonal phase stability in ZrO2 film formed on zirconium alloys and its effects on corrosion resistance. *Acta Mater* 55, 1695–1701. doi:10.1016/j.actamat.2006.10.030

Qin, W., Nam, C., Li, H. L., and Szpunar, J. A. (2007). Tetragonal phase stability in ZrO2 film formed on zirconium alloys and its effects on corrosion resistance. *Acta Mater* 55, 1695–1701. doi:10.1016/j.actamat.2006.10.030

Sabol, G., Kilp, G., Balfour, M., and Roberts, E. (1989). "Development of a cladding alloy for high burnup," in Zirconium in the Nuclear Industry: Eighth International Symposium, ASTM International, 100 Barr Harbor Drive, PO Box C700, West Conshohocken, PA, 227–244. 19428-2959. doi:10.1520/STP18868S

Samanta, A., Sawarn, T. K., Banerjee, S., Tyagi, A. K., and Bhasin, V. (2023). Susceptibility of Zr-2.5 (wt. %) Nb alloy to undergo nodular corrosion in water and steam environments: effect of surface, cold work, temperature. *Prog. Nucl. Energy* 163, 104823. doi:10.1016/j.pnucene.2023.104823

Sawabe, T., Sonoda, T., Furuya, M., Kitajima, S., and Takano, H. (2015). Residual stress distribution in oxide films formed on Zircaloy-2. *J. Nucl. Mater.* 466, 658–665. doi:10.1016/j.jnucmat.2015.08.040

Setiadinata, S. B. (2016). *Corrosion and hydrogen pickup mechanisms of zirconium alloys*.

Shebaldov, P., Peregud, M., Nikulina, A., Bibilashvili, Y., Lositski, A., Kuz'menko, N., et al. (2000). "E110 alloy cladding tube properties and their interrelation with alloy structure-phase condition and impurity content," in Zirconium in the Nuclear Industry: Twelfth International Symposium, ASTM International, 100 Barr Harbor Drive, PO Box C700, West Conshohocken, PA, 545–559. 19428-2959. doi:10.1520/STP14316S

Shukla, S., and Seal, S. (2005). Mechanisms of room temperature metastable tetragonal phase stabilisation in zirconia. *Int. Mater. Rev.* 50, 45–64. doi:10.1179/174328005X14267

Stein, F., Sauthoff, G., and Palm, M. (2002). Experimental determination of intermetallic phases, phase equilibria, and invariant reaction temperatures in the Fe-Zr system. *J. Phase Equilibria* 23, 480–494. doi:10.1361/105497102770331172

Steinbrueck, M., and Boettcher, M. (2011). Air oxidation of Zircaloy-4, M5 ®and ZIRLO™ cladding alloys at high temperatures. *J. Nucl. Mater.* 414, 276–285. doi:10.1016/j.jnucmat.2011.04.012

Sun, R., Xu, S., Yao, M., Zhang, J., Dai, X., Huang, J., et al. (2020). Effect of dissolved oxygen on corrosion behavior of Zr–0.85Sn–0.16Nb–0.37Fe–0.18Cr alloy in 500 °C and 10.3 MPa super-heated steam. *Trans. Nonferrous Metals Soc. China* 30, 701–709. doi:10.1016/S1003-6326(20)65247-5

Tejland, P., and Andren, F.-O. (2012). Origin and effect of lateral cracks in oxide scales formed on zirconium alloys. *J. Nucl. Mater.* 430, 64–71. doi:10.1016/j.jnucmat.2012.06.039

Vandegrift, J. L., Price, P. M., Stroud, J. P., Parga, C. J., Van Rooyen, I. J., Jaques, B. J., et al. (2019). Oxidation behavior of zirconium, zircaloy-3, zircaloy-4, Zr-1Nb, and Zr-2.5Nb in air and oxygen. *Nucl. Mater. Energy* 20, 100692. doi:10.1016/j.nme.2019.100692

Wagner, C. (1933). "Theory of ordered mixture phases. III," in *Appearances of irregularity in polar compounds as a basis for ion conduction and electron conduction*.

Wallwork, G. R., Rosa, C. J., and Smeltzer, W. W. (1965). Breakaway phenomena in the oxidation of zirconium at 850 and 950°C. *Corros. Sci.* 5 (113), 113–120. 120, IN5, IN10. doi:10.1016/s0010-938x(65)90471-3

Warr, B., Van Der Heide, P., and Maguire, M. (1996). "Oxide characteristics and corrosion and hydrogen uptake in Zr-2.5 Nb CANDU pressure tubes," in Zirconium in the Nuclear Industry: Eleventh International Symposium, ASTM International, 100 Barr Harbor Drive, PO Box C700, West Conshohocken, PA, 265–291. 19428-2959. doi:10.1520/STP16177S

Wei, J., Frankel, P., Polatidis, E., Blat, M., Ambard, A., Comstock, R. J., et al. (2013). The effect of Sn on autoclave corrosion performance and corrosion mechanisms in Zr-Sn-Nb alloys. *Acta Mater* 61, 4200–4214. doi:10.1016/j.actamat.2013.03.046

Weidinger, H., Ruhmann, H., Cheliotis, G., Maguire, M., and Yau, T.-L. (1991). "Corrosion-electrochemical properties of zirconium intermetallics," in Zirconium in the Nuclear Industry: Ninth International Symposium, ASTM International, 100 Barr Harbor Drive, PO Box C700, West Conshohocken, PA, 499–535. doi:10.1520/STP25525S

Whitney, E. D. (1965). Electrical resistivity and diffusionless phase transformations of zirconia at high temperatures and ultrahigh pressures. *J. Electrochem Soc.* 112, 91. doi:10.1149/1.2423476

Whitton, J. L. (1968). The measurement of ionic mobilities in the anodic oxides of tantalum and zirconium by a precision sectioning technique. *J. Electrochem Soc.* 115, 58. doi:10.1149/1.2411004

Wilhelm, A. N., and Garcia, E. A. (1987). Simulation of oxidation phenomena during high temperature transients: application to zirconium alloys in steam. *Mater. Sci. Eng.* 87, 73–79. doi:10.1016/0025-5416(87)90362-4

Xie, S., Zhou, B., Liang, X., Liu, W., Li, H., Li, Q., et al. (2017). A novel mechanism for nodular corrosion of Zircaloy-4 corroded in 773 K superheated steam. *Corros. Sci.* 126, 44–54. doi:10.1016/j.corsci.2017.06.007

Yilmazbayhan, A., Breval, E., Motta, A. T., and Comstock, R. J. (2006). Transmission electron microscopy examination of oxide layers formed on Zr alloys. *J. Nucl. Mater.* 349, 265–281. doi:10.1016/j.jnucmat.2005.10.012

Yilmazbayhan, A., Motta, A. T., Comstock, R. J., Sabol, G. P., Lai, B., and Cai, Z. (2004). Structure of zirconium alloy oxides formed in pure water studied with synchrotron radiation and optical microscopy: relation to corrosion rate. *J. Nucl. Mater.* 324, 6–22. doi:10.1016/j.jnucmat.2003.08.038

Yuan, R., Xie, Y. P., Li, T., Xu, C. H., Yao, M. Y., Xu, J. X., et al. (2021). An origin of corrosion resistance changes of Zr alloys: effects of Sn and Nb on grain boundary strength of surface oxide. *Acta Mater* 209, 116804. doi:10.1016/j.actamat.2021.116804

Zhao, W. (2001). Summary on out-of-pile and in-pile properties of M5 alloy. *Nucl. Power Eng.* 22, 60–64.

Zino, R., Chosson, R., Ollivier, M., Serris, E., and Favergeon, L. (2021). Parallel mechanism of growth of the oxide and α-Zr(O) layers on Zircaloy-4 oxidized in steam at high temperatures. *Corros. Sci.* 179, 109178. doi:10.1016/j.corsci.2020.109178